Research Article Vol. 30, No. 18 / 29 Aug 2022 / Optics Express 31913
Optics EXPRESS

Electrically switchable structural colors based on liquid-crystal-overlaid aluminum anisotropic nanoaperture arrays

KE LI,[1,2] JIAWEI WANG,[1] WENGFENG CAI,[1] HUILIN HE,[1,3] JIANXUN LIU,[1] ZHEN YIN,[1] DAN LUO,[1] QUANQUAN MU,[4] DAVY GÉRARD,[2,6] AND YAN JUN LIU[1,4,5,*]

[1]*Department of Electrical and Electronic Engineering, Southern University of Science and Technology, Shenzhen 518055, China*
[2]*Light, Nanomaterials, Nanotechnologies (L2n), Université de Technologie de Troyes & CNRS ERL 7004, 10004 Troyes, France*
[3]*Harbin Institute of Technology, Harbin 150001, China*
[4]*State Key Laboratory of Applied Optics, Changchun Institute of Optics, Fine Mechanics and Physics, Chinese Academy of Sciences, Changchun 130033, China*
[5]*Key Laboratory of Energy Conversion and Storage Technologies, Southern University of Science and Technology, Ministry of Education, Shenzhen 518055, China*
[6]*davy.gerard@utt.fr*
[*]*yjliu@sustech.edu.cn*

Abstract: Actively tunable or reconfigurable structural colors are highly promising in future development for high resolution imaging and displaying applications. To this end, we demonstrate switchable structural colors covering the entire visible range by integrating aluminum nanoaperture arrays with nematic liquid crystals. The geometrically anisotropic design of the nanoapertures provides strong polarization-dependent coloration. By overlaying a nematic liquid crystal layer, we further demonstrate switchable ability of the structural colors by either changing the polarization of the incident light or applying an external voltage. The switchable structural colors have a fast response time of 28 ms at a driving voltage of 6.5 V. Furthermore, colorful patterns are demonstrated by coding the colors with various dimensions of nanoaperture arrays with dual switching modes. Our proposed technique in this work provides a dual-mode switchable structural colors, which is highly promising for polarimetric displays, imaging sensors, and visual cryptography.

1. Introduction

Structural colors, originating from light-matter interactions, endow the characteristics of high resolution, reliability, nontoxicity, and durability compared with pigment-based traditional colors [1,2]. These advantageous features make structural colors an excellent candidate in high-resolution displays, photodetectors, imaging sensors, and high-density data storage [3–5]. Recently, thanks to the rapid development of advanced nanofabrication techniques, various structural colors, exploiting metallic or dielectric nanostructures [6–10], diffractive optical elements [11–16] and photonic crystals [17–21], have been adequately demonstrated. Generally, structural colors, dependent on the resonance in prefabricated geometry, suffer a restrained tunability. Consequently, to better satisfy the actual needs, it is highly desirable to further develop actively tunable or reconfigurable structural colors.

As known, the dimension of individual nanostructure, the lattice arrangement, and the surrounding medium are critical factors to the optical responses of nanostructures. Thus far, designing polarization-sensitive structures and exploiting active materials are two major approaches to achieve the color change. For instance, resonance-based colors based on anisotropic

#461887 https://doi.org/10.1364/OE.461887
Journal © 2022 Received 21 Apr 2022; revised 26 Jul 2022; accepted 8 Aug 2022; published 17 Aug 2022

Optics EXPRESS

nanostructures, such as nanoantennas and cross-shaped nanostructures, can be well tuned by changing the polarization of incident excitation light [22–24]. Structural colors can be also tuned by changing the refractive index of the surrounding medium around the nanostructures. Along this line, many phase-change materials have been introduced, for instances, liquid crystals (LCs) [24,25], VO_2 [26], Mg, and TiO_2 [27–29]. Of the aforesaid active media, LCs have large continuous variable refraction index, fast response speed, versatile driving schemes, and industry-compatible fabrication processes [30–34], which make them a superior candidate to generate actively tunable/reconfigurable structural colors. Recently, the LC-integrated nanostructured arrays have demonstrated about 100 nm-wavelength shift in the visible range [24,25,35–37]. However, structural colors that can be electrically switched on and off across the visible range have rarely been demonstrated.

Through deliberate design, high contrast can be achieved from anisotropic plasmonic nanoapertures for the incident light with two orthogonal polarizations [38–41]. Here, we demonstrate electrically switchable structural colors by integrating aluminum (Al) nanoapertures with nematic LCs. Full colors covering the whole visible range are achieved via changing the nanoaperture dimensions. These structural colors can be switched between a colorful state and a faded state by either applying an external electric field or changing the polarization direction of the incident light. Our experimental results suggest that the switchable structural colors have big potential for applications in polarimetric displays, imaging sensors, and visual cryptography.

2. Experimental section

2.1. Nanoaperture array fabrication

The nanoaperture array fabrication processes can be schematically described in Fig. S1 in the supplementary information. The polymethyl methacrylate (PMMA) solution (ARP672.045, 950k 4.5 wt% in anisole, Germany) was spin-coated on a cleaned indium-tin-oxide (ITO) glass using a spin coater (SUSS MicroTec-MA6/BA6, Germany). The coating speed is 5000 rpm/s with the acceleration of 500 rpm/s^2 for 60 s. The PMMA thickness was ~260 nm. Electron-beam lithography (EBL) (Nanobeam-nB5, England) was carried out with an exposure dose of 700 μC/cm^2. After that, the sample was developed for 65 s in a mixed developer solution including isopropyl alcohol (IPA) and methyl isobutyl ketone (MIBK) with a volume ratio of 3:1. To remove the residual gum after the development process and also strengthen the adhesion between the PMMA and Al layers, inductive coupled plasma (ICP) treatment (GSE200Plus, North Microelectronics Company, China) of the sample was further carried out for 10 s. Then a 50 nm-thick layer of Al was deposited using the direct current (DC) magnetron sputtering (KYKY-500CK-500ZF, KYKY Technology Co., Ltd., China). Finally, the Al nanoaperture arrays were fabricated. To assemble a LC cell, the ITO glass substrate with the Al nanoaperture arrays was further spin-coated another ultrathin layer of 5% diluted polyimide (PI) (5260T, Dalton, China) and then rubbed along the long axis of nanoaperture. We then assembled the nanoaperture arrays overlaid ITO glass substrate with another PI-coated one to form a twisted nematic (TN) LC cell. The cell gap was controlled to be 5 μm using the ball spacer. The nematic LC E7 (Jiangsu Hecheng Display Co., Ltd., China) was then injected into the cell by the capillary force on a heater at 70 °C, which is above the clearing point of LC, to eliminate the disturbance induced by the anisotropic elasticity.

2.2. Characterization

Surface morphologies of nanoaperture arrays were investigated by the field-emission scanning electron microscopy (FESEM) (GeminiSEM 300-71-10, Zeiss, Germany) with 5 kV at in-lens mode. The structural color palettes were characterized using a polarized optical microscope with an objective lens (magnification: 10x, numerical aperture: 0.3) (Nikon ‘pi’, Japan) equipped

Optics EXPRESS

with removable, rotatable polarizer and analyzer, and a halogen lamp source. The optical transmission spectra of the fabricated nanoaperture arrays were measured using a UV-Vis-NIR microspectrophotometer (20/30 PVTM, CRAIC Technologies, USA) at normal incidence with a 75 W broadband xenon source. All the transmission spectra were taken using air as the reference. The TN LC cell was driven by a square wave voltage with a frequency of 1 kHz, which was produced by a function generator (DG4102, Rigol, China). The response time of the TN LC cell was measured using a home-built setup include an oscilloscope (DPO2024, Tektronix, USA), detector (Model 2031, Newport, USA), and a single wavelength laser (REO 33361, Research Electro-Optics Co., USA) operating at 532 nm.

3. Results and discussion

Figure 1(a) illustrates the schematic design of polarization-dependent structural colors based on anisotropic nanoaperture arrays. The nanoaperture array is arranged in a square lattice with period P. The nanoapertures are rectangular with width W and length L. In our design, the aspect ratio of the nanoaperture is always fixed at $W/L = 1/2$. The thickness of the Al layer is 50 nm. We define the short and long axes of the nanoaperture as x- and y-axis, respectively, and θ as the polarization angle of the incident light with respect to the x-axis. Upon 0°-polarized incidence, enhanced transmission happens in the visible range due to the excitation of surface plasmon polaritons (SPPs). Upon 90°-polarized incidence, there is no obvious transmission in the visible range. As a result, the SPP-enhanced transmission is highly dependent on the geometric parameters of nanoaperture arrays. Therefore, the SPP resonance can be effectively tuned by changing the size and arrangement of nanoapertures. Hence, we achieved a color palette spanning the entire visible range under the 0°-polarized incidence, as shown Fig. 1(b). The fabricated nanoaperture arrays are arranged as follows: the period of the square lattice increases from 150 nm to 550 nm with the step size of 20 nm (from right to left in Fig. 1(b)) and the width of the nanoaperture varies from 50 nm to 250 nm with the step size of 20 nm (from bottom to top in Fig. 1(b)). In contrast, when we rotate the polarization direction by 90°, the nanoaperture arrays demonstrate a significant decrease of the light transmission with only a faded blue color, as shown in Fig. 1(c). Figure 1(b) and 1(c) were observed under a polarizing optical microscope and taken with an equipped CCD. The created structural colors in Fig. 1(b) were also calibrated in the CIE 1931 color space, as shown in Fig. 1(d), showing that we have successfully achieved the full-color gamut. The slight discrepancy of color performance between Fig. 1(b) and 1(d) stems from the different sources, in which D65 is exploited in the CIE 1931, while a halogen lamp is used in our experiment [42].

Spectral and morphological characterizations were carried out on the fabricated nanostructures. Figure 2(a) and 2(b) present 0°- and 90°-polarized transmission spectra of the fabricated nanoaperture arrays. The width and period of the nanoaperture arrays were changed from 90/270 to 190/470 nm with the increasing step size of 20/40 nm, respectively. The corresponding SEM images show good quality of surface morphologies, as shown in Fig. 2(c)–2(h). The measured size of the nanoapertures is slightly smaller than the designed value, owing to an experimental error during the fabrication processes. Comparing Fig. 2(a) and 2(b), the nanoaperture arrays demonstrate a single additive color due to the SPP excitation only upon the 0°-polarized incidence. By changing both the nanoaperture size and array period, the resonance center wavelength can be effectively tuned from 400 to 700 nm, covering the entire visible spectrum.

The transmission peaks can be mainly attributed to the light-excited SPPs subject to the momentum match with the additional momentum provided by periodic nanoaperture arrays [43–45]. In this way, with the fixed nanoaperture width, the resonance center wavelength changes linearly with the array period, as shown in Supplement 1, Fig. S2. In addition, the existence of Rayleigh anomalies (associated with the emergence or disappearance of diffracted orders) results in a transmission minimum and an asymmetric optical shape, as shown in Supplement 1, Fig. S3

Optics EXPRESS

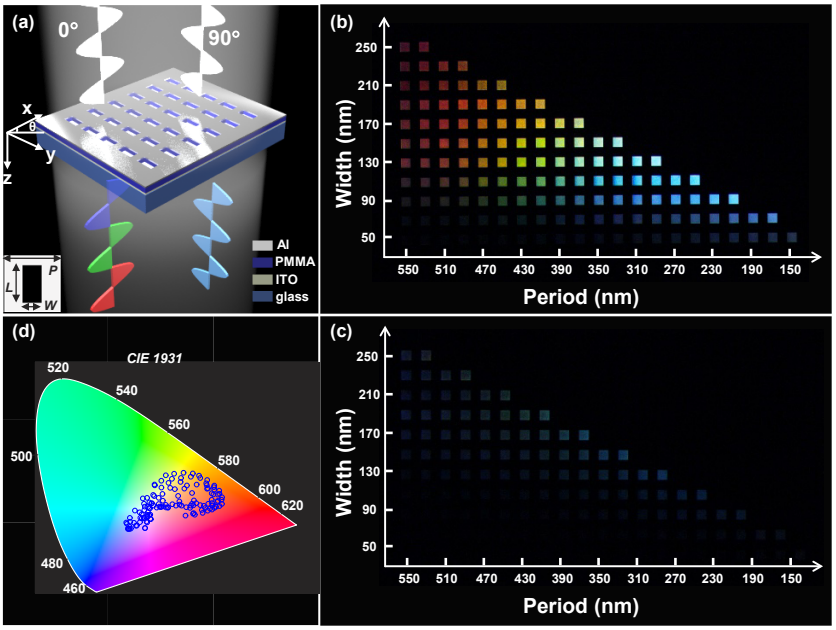

Fig. 1. (a) Schematic design of polarization-dependent structural colors based on anisotropic Aluminum nanoaperture arrays. The left bottom inset shows the structural parameters, *W*, *L*, and *P*, of the nanoaperture array that represent the width and length of nanoaperture, and nanoaperture array period, respectively. The color palettes illuminated by 0°- (b) and 90°-polarized (c) light. (d) Corresponding positions plotted in the CIE1931 color space for the created structural colors illustrated in (b).

[45–50]. As expected for Rayleigh anomalies, the spectra have the same minimum position when they have the same periodicity [51]. Upon 90°-polarized incidence, the nanoaperture arrays demonstrate extremely low transmission, which is attributed to the low coupling efficiency of SPPs at the top and bottom interfaces along the long axis of the nanoapertures in square lattice [38,39], as shown in Fig. 2(b). They only exhibit a pale blue appearance for all the nanoaperture arrays [45,52]. To evaluate the lifetime of SPPs, we extract the full width at half maximum (FWHM) with the parameters as shown in Supplement 1, Fig. S3. Increased nanoaperture size enhances the inelastic collision of electrons, shortening the propagation distance and lifetime of the SPPs, as shown in Supplement 1, Fig. S4. The propagation length is in the range of 1.2 to 2 μm for the arrays with the parameters in Fig. S3, depending on the resonance position [53,54].

Furthermore, we measured the transmission spectra for the nanoaperture array with $W = 190$ nm and $P = 550$ nm as a function of the incident polarization angle changing from 0° to 90° with a step size of 15°, as shown in Supplement 1, Fig. S5a. The transmittance changes significantly with the incident polarization angle, demonstrating maximum and minimum values when the polarization is parallel and perpendicular to the short axis of the nanoapertures (i.e., the *x*-axis), respectively. At the plasmonic resonance of ~684 nm, the change of the transmittance with the incident polarization angle can be well fitted with a half-cycle sinusoidal curve (see Supplement 1, Fig. S5b), demonstrating a potentially useful approach to determine the linear polarization direction of the incident light by interpolating the signal. Similar to the reported work [55], another kind of compact detector with ultra-high resolution, simultaneously obtaining spectral and polarization information, could be achieved through overlapping different periodic nanoapertures at a certain angle. The color polarimetry is a promising technique in many fields, such as remote sensing, target recognition, optical anti-counterfeiting [56–58].

Optics EXPRESS

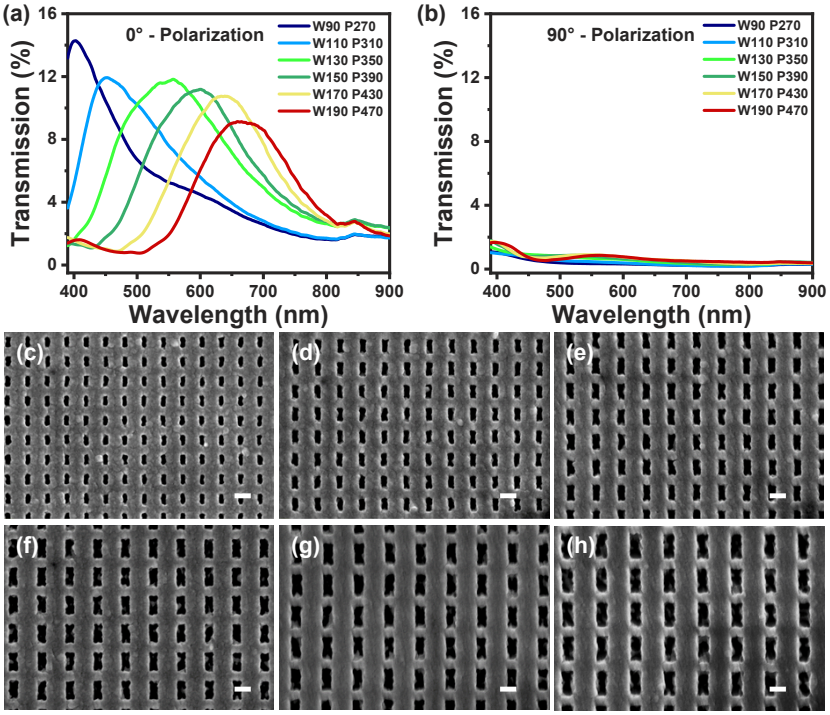

Fig. 2. (a) 0°- and (b) 90°-polarized transmission spectra of the fabricated nanoaperture arrays. Typical SEM images of the nanoaperture arrays with the nanoaperture width and array period being (c) 90 and 270 nm, (d) 110 and 310 nm, (e) 130 and 350 nm, (f) 150 and 390 nm, (g) 170 and 430 nm, and (h) 190 and 470 nm, respectively. Scale bar: 200 nm.

In the following, we demonstrate active control of the transmitted colors by assembling the fabricated nanoaperture arrays onto an ITO glass substrate with another PI-coated one to form a TN LC cell. The alignment quality of LC molecules inside the TN cell was investigated using polarized optical microscopy with two parallel (Supplement 1, Fig. S6) and crossed polarizers (Supplement 1, Fig. S7). As known, when the incident light with its polarization parallel to the alignment direction passes through from one side to the other of the TN cell, the light polarization will rotate 90° along with the twist of LC director due to the well-known Mauguin effect [59,60]. Therefore, the TN LC cell demonstrates a totally dark state under two parallel polarizers (Supplement 1, Fig. S6a and S6b) and a bright colored state under two crossed polarizers (Supplement 1, Fig. S7a and S7b). In contrast, upon application of a sufficient voltage, the LC molecules will re-orientate along the electric field direction and the twist will disappear accordingly. As a result, the incident light polarization does not rotate and the TN LC cell demonstrates an opposite appearance, as shown in Supplement 1, Fig. S6c and S6d, and Fig. S7c and S7d, respectively. From Supplement 1, Fig. S6 and S7, we can confirm that a high-quality TN LC alignment has been achieved with the nanoaperture arrays. Meanwhile, the structural colors still exist with the LC overlayer. This lays the foundation that we could use the LC to switch the structural colors.

By overlaying LCs on the nanoaperture arrays, their optical responses were further characterized. Figure 3 illustrates the schematic design and experimental results of electrically switchable structural colors. From Fig. 3(a) and 3(b), the 0°- and 90°-polarized incident light for the nanoaperture arrays can be interchanged by switching the LC alignment with an externally

Optics EXPRESS

applied voltage. Figure 3(c) and 3(d) demonstrate the rotation effect of TN LCs when the light is incident from the PI-coated ITO glass side, as shown in Fig. 3(a), in which 90°-polarized incident light can excite SPP-activated color rendering, whereas 0°-polarized incident light only gives faded blue color. In such a case, the TN LC-overlaid nanoaperture arrays render an inverse polarization-dependent color palette compared to the bare ones. Upon applying a voltage of 10 V, the re-orientation of LC molecules causes the disappearance of the twist and the LC-overlaid nanoaperture arrays demonstrate an opposite switch effect of the structural colors, as shown in Fig. 3(e) and 3(f).

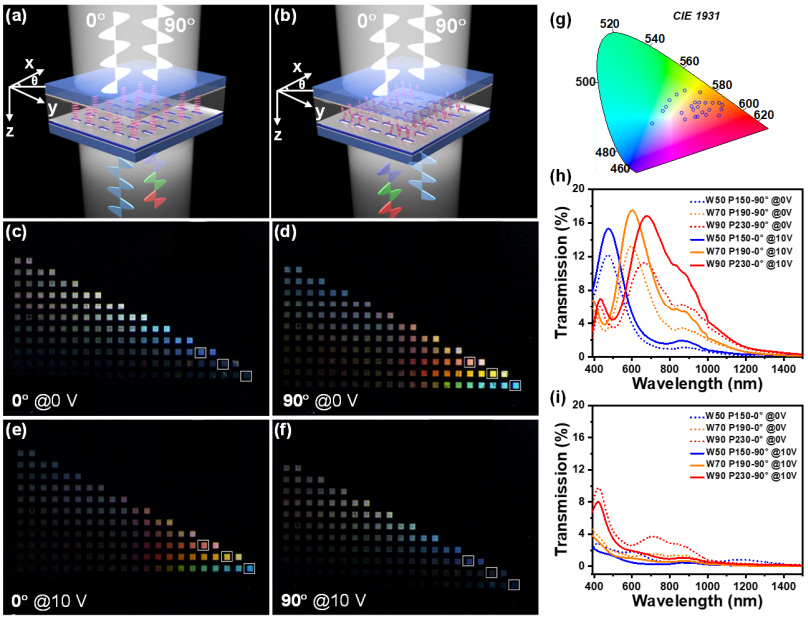

Fig. 3. Schematic of electrically switchable structural colors inside a TN LC cell before (a) and after (b) electric driving. Polarized optical microscopy images under 0°- (c, e) and 90°-polarized (d, f) incidence at 0 V (c, d) and 10 V (e, f), respectively. (g) Corresponding positions plotted in the CIE1931 color space for the color palette illustrated in (d). (h) Optical transmission spectra of nanoaperture arrays labeled with the white squares in (d) and (e). (i) Optical transmission spectra of nanoaperture arrays labeled with the white squares in (c) and (f).

Comparing Fig. 3(d) and Fig. 1(b), which correspond to nanoaperture arrays having the same dimensions, all structural colors exhibit a clear redshift due to the refractive index change caused by the LC overlayer. For the same nanoaperture arrays with their transmission spectra demonstrated in Fig. 2(a) and 2(b), the spectral changes upon LC infiltration can be clearly observed in Supplement 1, Fig. S8. The achieved structural colors after LC infiltration in Fig. 3(d) are also calibrated in the CIE 1931 color space, as shown in Fig. 3(g), which covers the same range as the bare nanoaperture arrays. Upon application of an external electric field, 0°-polarized structural colors in Fig. 3(e) are almost the same as the 90°-polarized ones at 0 V in Fig. 3(d), which can be further verified by the measured transmission spectra in Fig. 3(h) by selecting three typical nanoaperture arrays labeled with white squares in Fig. 3(d) and 3(e). From Fig. 3(h), their spectra are similar except for a slight difference in intensity. The transmittance for blue, yellow, pink can reach ~16%, a quite high value for the nanoapertures benefiting from the EOT effect [44]. Similarly, the 90°-polarized structural colors in Fig. 3(f) are almost identical to the 0°-polarized ones from Fig. 3(c), which can be verified in the measured transmission spectra

Optics EXPRESS

from Fig. 3(i) by selecting the same nanoaperture arrays labeled with white squares in Fig. 3(c) and 3(f). As a result, electrically switchable structural colors can be achieved by interchanging the incident light polarization via the LC re-orientation.

Switching speed is another key parameter for the actively tunable/reconfigurable structural colors. Therefore, the response time of our switchable structural colors was further investigated. Figure 4(a) shows measured transmission spectra as a function of the applied voltage for one nanoaperture array with the nanoaperture width and array period of 50 and 150 nm, respectively. As the applied voltage increases, the 0°-polarized plasmonic resonance peak gradually increases due to the de-twist of LC molecules. The inset in Fig. 4(a) shows the normalized transmission versus the applied voltage at the wavelength of 400 nm, in good agreement with the electro-optical curve of typical TN LC cells [61]. From the inset in Fig. 4(a), the measured threshold and switching voltages are 2.9 and 4.2 V, respectively. We then applied a voltage above the switching one to drive the sample to measure the response time of the TN LC cell using a home-made system (see details in Experimental section). Figure 4(b) shows the measured rising (red curve) and falling (green curve) time at the applied voltage of 4.2 V. The detailed data are listed in Table S1 and Fig. S9 in Supplement 1. The optimal rising and falling times are 11.2 and 16.79 ms, respectively, resulting in the total response time of ~28 ms at a driving voltage of 6.5 V, which is much faster than the reported work based on a chemical reaction [27–29].

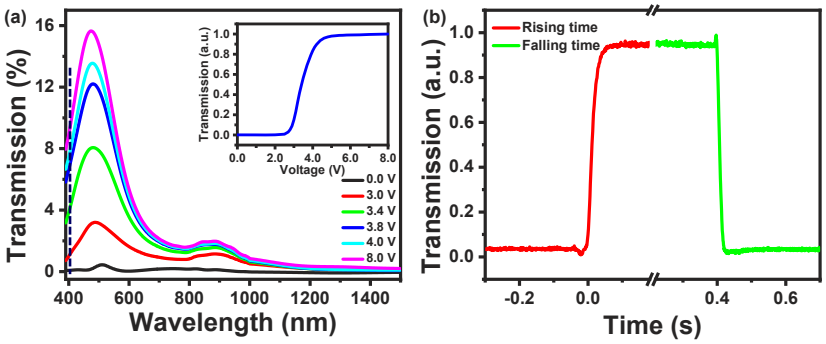

Fig. 4. (a) Optical transmission spectra as a function of the applied voltage for the nanoaperture array with $W = 50$ nm and $P = 150$ nm. Inset shows the normalized transmission versus applied voltage at the fixed wavelength of 400 nm marked with a vertical dash line in the spectra. (b) Experimentally measured rising and falling time at the applied voltage of 4.2 V.

Structural colors based on nanoaperture arrays is a highly promising enabling technology for ultrahigh-resolution display applications. Figure 5 exhibits the resolution patterns of the three primary red (R), green (G), and blue (B) plasmonic colors. We have achieved the smallest color pixel with a 2×2 array of nanoapertures, resulting in a high resolution of ~27,000, 30,000, and 60,000 dpi (dots per inch) for the R, G, and B colors, respectively. For the practical applications, in addition to resolution, the most efficient EOT of array with dimensions larger than the SPP propagation length should be also considered when necessary to achieve the optimal performance [53,54]. Sometimes, due to the edge effect of the finite array, the nonuniformity of the coloring can be eliminated at moderate incident angles that do not cause large changes in momentum compensation [62].

As a proof-of- concept, we have designed and fabricated two passive patterns (“mandarin duck” and “rainbow”) based on our color database, as shown in Fig. 6. Figure 6(a) and 6(d) illustrate the SEM morphologies for the two patterns. 0°- and 90°-polarized patterns are displayed in Fig. 6(b) and 6e, and Fig. 6(c) and 6(f), respectively. As a result, we can not only achieve colorful images under 0°-polarized illumination but also hide them by rotating the polarization direction of 90°.

Optics EXPRESS

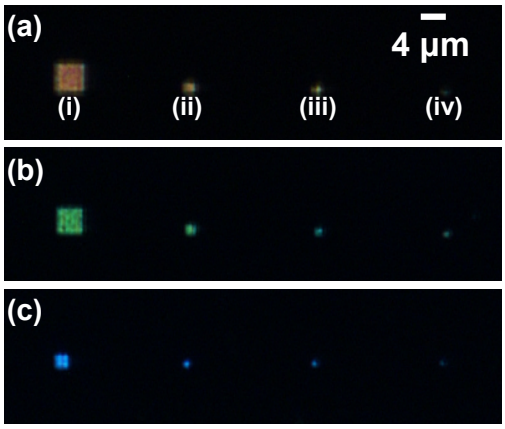

Fig. 5. Resolution testing pattern excited by 0°-polarized incidence based on the Al nanoapertures for red (a), green (b), and blue (c) colors with the width of 170/110/90 nm and period of 470/410/210 nm, respectively. (i–iv) The square patterns consist of a 10×10, 4×4, 3×3, 2×2 array of nanoapertures, respectively.

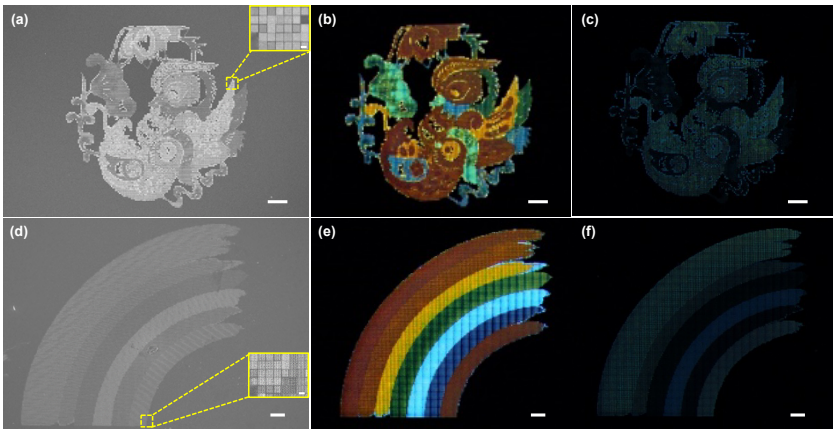

Fig. 6. Two designed "duck" and "rainbow" patterns using our color mapping scheme based on the bare nanoaperture arrays to experimentally verify the color palette switch effect. The corresponding top-view SEM (a, d) and captured microscopic images under the 0°- (b, e) and 90°-polarized (c, f) illumination. Scale bar: 40 μm and inset scale bar: 2 μm.

Optics EXPRESS

Assembling the TN LC cell with the above patterns, no switchable chromatic image can be seen due to the color redshift caused by the LC overlayer. We further re-encoded a snowflake image using the LC-based color database in Fig. 3. Figure 7(a) and 7(b) show the 0°- and 90°-polarized images without applying a voltage. Upon applying a voltage, the 0°- and 90°-polarized images are inversely switched. In this way, one can achieve dual-mode switchable images by either changing the polarization of the incident light or applying an external voltage, which could be potentially useful in encryption.

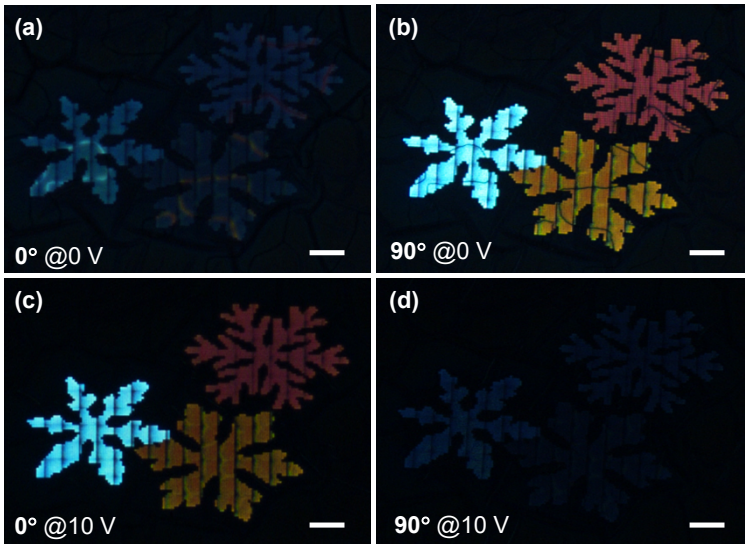

Fig. 7. The designed "snowflake" pattern using our color mapping scheme based on the LC overlaid nanoaperture arrays to experimentally verify electrically switchable color effect. Optical microscopic images captured at applied voltages of 0 V (a, b) and 10 V (c, d) under the 0°- (a, c) and 90°-polarized (b, e) illumination. Scale bar: 40 μm.

4. Conclusion

In summary, we have achieved structural colors covering the entire visible range by integrating aluminum nanoaperture arrays with nematic LCs. The geometrically anisotropic design of the nanoapertures gave rise to a polarization-dependent coloration. By overlaying a nematic LC layer, we achieved switchability of the structural colors by either changing the polarization of the incident light or by applying an external voltage. The switchable structural colors have a fast response time of 28 ms at a driving voltage of 6.5 V. Furthermore, vivid colorful patterns have been demonstrated by encoding the colors with various dimensions of nanoaperture arrays with dual switching modes. The proposed technique provides dual-mode switchable structural colors, which is highly promising for imaging and displaying applications, such as visual cryptography, security labels, imaging sensors, and ultrahigh-resolution displays.

Funding. National Natural Science Foundation of China (62075093, 62211530039); Guangdong Province Introduction of Innovative R&D Team (2017ZT07C071); Natural Science Foundation of Guangdong Province (2019A1515110864); Science, Technology and Innovation Commission of Shenzhen Municipality (GJHZ20180928155207206, JCYJ20170817111349280, JCYJ20180305180635082); Open Fund of State Key Laboratory of Applied Optics (SKLAO-201904).

Acknowledgments. The authors also acknowledge the assistance of SUSTech Core Research Facilities.

Disclosures. The authors declare no conflicts of interest.

Data availability. Data underlying the results presented in this paper are not publicly available at this time but may be obtained from the authors upon reasonable request.

Optics EXPRESS

Supplemental document. See Supplement 1 for supporting content.

References

1. A. Kristensen, J. K. W. Yang, S. I. Bozhevolnyi, S. Link, P. Nordlander, N. J. Halas, and N. A. Mortensen, "Plasmonic colour generation," Nat. Rev. Mater. **2**(1), 16088 (2017).
2. A. I. Kuznetsov, A. E. Miroshnichenko, M. L. Brongersma, Y. S. Kivshar, and B. Luk'yanchuk, "Optically resonant dielectric nanostructures," Science **354**(6314), aag2472 (2016).
3. P. R. Wiecha, A. Arbouet, C. Girard, A. Lecestre, G. Larrieu, and V. Paillard, "Evolutionary multi-objective optimization of colour pixels based on dielectric nanoantennas," Nat. Nanotechnol. **12**(2), 163–169 (2017).
4. N. S. King, L. Liu, X. Yang, B. Cerjan, H. O. Everitt, P. Nordlander, and N. J. Halas, "Fano resonant aluminum nanoclusters for plasmonic colorimetric sensing," ACS Nano **9**(11), 10628–10636 (2015).
5. M. Jiang, S. Y. Siew, J. Y. E. Chan, J. Deng, Q. Y. S. Wu, L. Jin, J. K. W. Yang, J. Teng, A. Danner, and C.-W. Qiu, "Patterned resist on flat silver achieving saturated plasmonic colors with sub-20-nm spectral linewidth," Mater. Today **35**, 99–105 (2020).
6. K. Kumar, H. Duan, R. S. Hegde, S. C. W. Koh, J. N. Wei, and J. K. W. Yang, "Printing colour at the optical diffraction limit," Nat. Nanotechnol. **7**(9), 557–561 (2012).
7. G. Si, Y. Zhao, J. Lv, M. Lu, F. Wang, H. Liu, N. Xiang, T. J. Huang, A. J. Danner, J. Teng, and Y. J. Liu, "Reflective plasmonic color filters based on lithographically patterned silver nanorod arrays," Nanoscale **5**(14), 6243–6248 (2013).
8. G. Si, Y. Zhao, E. S. P. Leong, J. Lv, and Y. J. Liu, "Incident-angle dependent color tuning from a single plasmonic chip," Nanotechnology **25**(45), 455203 (2014).
9. L. Duempelmann, A. Luu-Dinh, B. Gallinet, and L. Novotny, "Four-fold color filter based on plasmonic phase retarder," ACS Photonics **3**(2), 190–196 (2016).
10. H. Yun, S.-Y. Lee, K. Hong, J. Yeom, and B. Lee, "Plasmonic cavity-apertures as dynamic pixels for the simultaneous control of colour and intensity," Nat. Commun. **6**(1), 7133 (2015).
11. L. Cao, P. Fan, E. S. Barnard, A. M. Brown, and M. L. Brongersma, "Tuning the Color of Silicon Nanostructures," Nano Lett. **10**(7), 2649–2654 (2010).
12. X. Zhu, W. Yan, U. Levy, N. A. Mortensen, and A. Kristensen, "Resonant laser printing of structural colors on high-index dielectric metasurfaces," Sci. Adv. **3**(5), e1602487 (2017).
13. S. Sun, Z. Zhou, C. Zhang, Y. Gao, Z. Duan, S. Xiao, and Q. Song, "All-Dielectric Full-Color Printing with TiO2 Metasurfaces," ACS Nano **11**(5), 4445–4452 (2017).
14. W. Yang, S. Xiao, Q. Song, Y. Liu, Y. Wu, S. Wang, J. Yu, J. Han, and D.-P. Tsai, "All-dielectric metasurface for high-performance structural color," Nat. Commun. **11**(1), 1864 (2020).
15. H. Liu, D. Quan, K. Li, Y. Zheng, F. Lou, S. Liu, Y. Liu, A. K. Srivastava, G. Li, C. Qiu, Z. Liu, and X. Cheng, "Dielectric Metasurface from Solution-Phase Epitaxy of ZnO Nanorods for Subtractive Color Filter Application," Adv. Opt. Mater. **9**(5), 2001670 (2021).
16. A. A. High, R. C. Devlin, A. Dibos, M. Polking, D. S. Wild, J. Perczel, N. P. de Leon, M. D. Lukin, and H. Park, "Visible-frequency hyperbolic metasurface," Nature **522**(7555), 192–196 (2015).
17. M. Qi, E. Lidorikis, P. T. Rakich, S. G. Johnson, J. D. Joannopoulos, E. P. Ippen, and H. I. Smith, "A three-dimensional optical photonic crystal with designed point defects," Nature **429**(6991), 538–542 (2004).
18. Y. Liu, H. Wang, J. Ho, R. C. Ng, R. J. H. Ng, V. H. Hall-Chen, E. H. H. Koay, Z. Dong, H. Liu, C.-W. Qiu, J. R. Greer, and J. K. W. Yang, "Structural color three-dimensional printing by shrinking photonic crystals," Nat. Commun. **10**(1), 4340 (2019).
19. H. Jiang, W. Cai, K. Li, M. Cheng, V. Kumar, Z. Yin, D. Gérard, D. Luo, Q. Mu, and Y. Liu, "Holographically fabricated, highly reflective nanoporous polymeric distributed Bragg reflectors with red, green, and blue colors," Chin. Opt. Lett. **18**(8), 080007 (2020).
20. L. Wang, A. M. Urbas, and Q. Li, "Nature-inspired emerging chiral liquid crystal nanostructures: from molecular self-assembly to DNA mesophase and nanocolloids," Adv. Mater. **32**(41), 1801335 (2020).
21. Y. Yang, L. Wang, H. Yang, and Q. Li, "3D Chiral Photonic Nanostructures Based on Blue-Phase Liquid Crystals," Small Science **1**(6), 2100007 (2021).
22. A. Kumar, Y. K. Srivastava, M. Manjappa, and R. Singh, "Color-Sensitive Ultrafast Optical Modulation and Switching of Terahertz Plasmonic Devices," Adv. Opt. Mater. **6**(15), 1800030 (2018).
23. Z. Li, W. Wang, D. Rosenmann, D. A. Czaplewski, X. Yang, and J. Gao, "All-metal structural color printing based on aluminum plasmonic metasurfaces," Opt. Express **24**(18), 20472 (2016).
24. Y. Lee, M.-K. Park, S. Kim, J. H. Shin, C. Moon, J. Y. Hwang, J.-C. Choi, H. Park, H.-R. Kim, and J. E. Jang, "Electrical broad tuning of plasmonic color filter employing an asymmetric-lattice nanohole array of metasurface controlled by polarization rotator," ACS Photonics **4**(8), 1954–1966 (2017).
25. M. Sharma, N. Hendler, and T. Ellenbogen, "Electrically switchable color tags based on active liquid-crystal plasmonic metasurface platform," Adv. Opt. Mater. **8**(7), 1901182 (2020).
26. F.-Z. Shu, F.-F. Yu, R.-W. Peng, Y.-Y. Zhu, B. Xiong, R.-H. Fan, Z.-H. Wang, Y. Liu, and M. Wang, "Dynamic plasmonic color generation based on phase transition of vanadium dioxide," Adv. Opt. Mater. **6**(7), 1700939 (2018).
27. X. Duan and N. Liu, "Scanning plasmonic color display," ACS Nano **12**(8), 8817–8823 (2018).

Optics EXPRESS

28. M. Huang, A. J. Tan, F. Büttner, H. Liu, Q. Ruan, W. Hu, C. Mazzoli, S. Wilkins, C. Duan, J. K. W. Yang, and G. S. D. Beach, "Voltage-gated optics and plasmonics enabled by solid-state proton pumping," Nat. Commun. **10**(1), 5030 (2019).
29. Y. Wu, W. Yang, Y. Fan, Q. Song, and S. Xiao, "TiO2 metasurfaces: from visible planar photonics to photochemistry," Sci. Adv. **5**(11), eaax0939 (2019).
30. Y. J. Liu, Q. Hao, J. S. T. Smalley, J. Liou, I. C. Khoo, and T. J. Huang, "A frequency-addressed plasmonic switch based on dual-frequency liquid Crystals," Appl. Phys. Lett. **97**(9), 091101 (2010).
31. Y. J. Liu, Y. B. Zheng, J. Liou, I.-K. Chiang, I. C. Khoo, and T. J. Huang, "All-optical modulation of localized surface plasmon coupling in a hybrid system composed of photoswitchable gratings and Au nanodisk arrays," J. Phys. Chem. C **115**(15), 7717–7722 (2011).
32. Y. J. Liu, G. Y. Si, E. S. P. Leong, B. Wang, A. J. Danner, X. C. Yuan, and J. H. Teng, "Optically tunable plasmonic color filters," Appl. Phys. A **107**(1), 49–54 (2012).
33. Y. J. Liu, G. Y. Si, E. S. P. Leong, N. Xiang, A. J. Danner, and J. H. Teng, "Light-driven plasmonic color filters by overlaying photoresponsive liquid crystals on gold annular aperture arrays," Adv. Mater. **24**(23), OP131–OP135 (2012).
34. G. Y. Si, Y. H. Zhao, E. S. P. Leong, and Y. J. Liu, "Liquid-crystal-enabled active plasmonics: a review," Materials **7**(2), 1296–1317 (2014).
35. D. Franklin, Z. He, P. M. Ortega, A. Safaei, P. Cencillo-Abad, S.-T. Wu, and D. Chanda, "Self-assembled plasmonics for angle-independent structural color displays with actively addressed black states," Proc. Natl. Acad. Sci. U.S.A. **117**(24), 13350–13358 (2020).
36. D. Franklin, Y. Chen, A. Vazquez-Guardado, S. Modak, J. Boroumand, D. Xu, S.-T. Wu, and D. Chanda, "Polarization-independent actively tunable colour generation on imprinted plasmonic surfaces," Nat. Commun. **6**(1), 7337 (2015).
37. D. Franklin, R. Frank, S.-T. Wu, and D. Chanda, "Actively addressed single pixel full-colour plasmonic display," Nat. Commun. **8**(1), 15209 (2017).
38. R. Gordon, A. G. Brolo, A. McKinnon, A. Rajora, B. Leathem, and K. L. Kavanagh, "Strong Polarization in the Optical Transmission through Elliptical Nanohole Arrays," Phys. Rev. Lett. **92**(3), 037401 (2004).
39. K. J. K. Koerkamp, S. Enoch, F. B. Segerink, N. F. van Hulst, and L. Kuipers, "Strong Influence of Hole Shape on Extraordinary Transmission through Periodic Arrays of Subwavelength Holes," Phys. Rev. Lett. **92**(18), 183901 (2004).
40. K. L. van der Molen, K. J. K. Koerkamp, S. Enoch, F. B. Segerink, N. F. van Hulst, and L. Kuipers, "Role of shape and localized resonances in extraordinary transmission through periodic arrays of subwavelength holes: experiment and theory," Phys. Rev. B: Condens. Matter Mater. Phys. **72**(4), 045421 (2005).
41. X.-F. Ren, P. Zhang, G.-P. Guo, Y.-F. Huang, Z.-W. Wang, and G.-C. Guo, "Polarization properties of subwavelength hole arrays consisting of rectangular holes," Appl. Phys. B **91**(3-4), 601–604 (2008).
42. P. Mao, C. Liu, F. Song, M. Han, S. A. Maier, and S. Zhang, "Manipulating disordered plasmonic systems by external cavity with transition from broadband absorption to reconfigurable reflection," Nat. Commun. **11**(1), 1538 (2020).
43. T. W. Ebbesen, H. J. Lezec, H. F. Ghaemi, T. Thio, and P. A. Wolff, "Extraordinary optical transmission through sub-wavelength hole arrays," Nature **391**(6668), 667–669 (1998).
44. C. Genet and T. W. Ebbesen, "Light in tiny holes," Nature **445**(7123), 39–46 (2007).
45. S.-H. Chang, S. K. Gray, and G. C. Schatz, "Surface plasmon generation and light transmission by isolated nanoholes and arrays of nanoholes in thin metal films," Opt. Express **13**(8), 3150–3165 (2005).
46. R. W. Wood, "On a remarkable case of uneven distribution of light in a diffraction grating spectrum," Proc. Phys. Soc. London **18**(1), 269–275 (1902).
47. A. A. Maradudin, I. Simonsen, J. Polanco, and R. M. Fitzgerald, "Rayleigh and Wood anomalies in the diffraction of light from a perfectly conducting reflection grating," J. Opt. **18**(2), 024004 (2016).
48. D. Khlopin, F. Laux, W. P. Wardley, J. Martin, G. A. Wurtz, J. Plain, N. Bonod, A. V. Zayats, W. Dickson, and D. Gérard, "Lattice modes and plasmonic linewidth engineering in gold and aluminum nanoparticle arrays," J. Opt. Soc. Am. B **34**(3), 691–700 (2017).
49. E. S. H. Kang, H. Ekinge, and M. P. Jonsson, "Plasmonic fanoholes: on the gradual transition from suppressed to enhanced optical transmission through nanohole arrays in metal films of increasing film thickness," Opt. Mater. Express **9**(3), 1404–1415 (2019).
50. B. Malekian, K. Xiong, E. S. H. Kang, J. Andersson, G. Emilsson, M. Rommel, T. Sannomiya, M. P. Jonsson, and A. Dahlin, "Optical properties of plasmonic nanopore arrays prepared by electron beam and colloidal lithography," Nanoscale Adv. **1**(11), 4282–4289 (2019).
51. R. Adato, A. A. Yanik, J. J. Amsden, D. L. Kaplan, F. G. Omenetto, M. K. Hong, S. Erramilli, and H. Altug, "Ultra-sensitive vibrational spectroscopy of protein monolayers with plasmonic nanoantenna arrays," Proc. Natl. Acad. Sci. U.S.A. **106**(46), 19227–19232 (2009).
52. T. Nakanishi, E. Tsutsumi, K. Masunaga, A. Fujimoto, and K. Asakawa, "Transparent aluminum nanomesh electrode fabricated by nanopatterning using self-assembled nanoparticles," Appl. Phys. Express **4**(2), 025201 (2011).
53. D. S. Kim, S. C. Hohng, V. Malyarchuk, Y. C. Yoon, Y. H. Ahn, K. J. Yee, J. W. Park, J. Kim, Q. H. Park, and C. Lienau, "Microscopic origin of surface-plasmon radiation in plasmonic band-gap nanostructures," Phys. Rev. Lett. **91**(14), 143901 (2003).

Optics EXPRESS

54. F. Przybilla, A. Degiron, C. Genet, T. W. Ebbesen, F. de Léon-Pérez, J. Bravo-Abad, F. J. García-Vidal, and L. Martín-Moreno, "Efficiency and finite size effects in enhanced transmission through subwavelength apertures," Opt. Express **16**(13), 9571–9579 (2008).
55. E. Laux, C. Genet, T. Skauli, and T. W. Ebbesen, "Plasmonic photon sorters for spectral and polarimetric imaging," Nat. Phys. **2**(3), 161–164 (2008).
56. V. Kaushik, S. Rajput, S. Srivastav, L. Singh, P. Babu, E. Heidari, M. Ahmed, Y. Al-Hadeethi, H. Dalir, V. J. Sorger, and M. Kumar, "On-chip nanophotonic broadband wavelength detector with 2D-Electron gas," Nanophotonics **11**(2), 289–296 (2022).
57. K. Li, J. Wang, W. Cai, H. He, M. Cen, J. Liu, D. Luo, Q. Mu, D. Gérard, and Y. J. Liu, "Electrically switchable, polarization-sensitive encryption based on aluminum nanoaperture arrays integrated with polymer-dispersed liquid crystals," Nano Lett. **21**(17), 7183–7190 (2021).
58. J. Wang, K. Li, H. He, W. Cai, J. Liu, Z. Yin, Q. Mu, V. K. S. Hsiao, D. Gérard, D. Luo, G. Li, and Y. J. Liu, "Metasurface-enabled high-resolution liquid-crystal alignment for display and modulator applications," Laser Photon. Rev. **16**(1), 2100396 (2022).
59. D. W. Berreman, "Liquid-crystal twist cell dynamics with backflow," J. Appl. Phys. **46**(9), 3746–3751 (1975).
60. M. Schadt, "Milestone in the history of field-effect liquid crystal displays and materials," Jpn. J. Appl. Phys. **48**(3), 03B001 (2009).
61. Y. B. Kim and I. K. Hur, "High speed response time of nematic liquid crystal mixtures for LCD monitor and TV applications," J. Inf. Disp. **2**(3), 32–38 (2001).
62. J. Bravo-Abad, A. Degiron, F. Przybilla, C. Genet, F. J. García-Vidal, L. Martín-Moreno, and T. W. Ebbesen, "How light emerges from an illuminated array of subwavelength holes," Nat. Phys. **2**(2), 120–123 (2006).